Sensors and Materials, Vol. 38, No. 1 (2026) 363–373
MYU Tokyo

S & M 4304

Design of a Dual-axis Solar Tracking Mechanism

Sean Te-Hsun Lin,[1] Xiao-Qing Lin,[2] Wei-Ling Hsu,[3]
Chao-Ming Hsu,[2*] and Cheng-Fu Yang[4,5**]

[1]School of Economics and Management, Jiaying University, Meizhou 514015, Guangdong, China
[2]Department of Mechanical Engineering, National Kaohsiung University of Science and Technology, Kaohsiung 807, Taiwan
[3]School of Civil Engineering, Jiaying University, Meizhou 514015, Guangdong, China
[4]Department of Chemical and Materials Engineering, National University of Kaohsiung, Kaohsiung 811, Taiwan
[5]Department of Aeronautical Engineering, Chaoyang University of Technology, Taichung 413, Taiwan

(Received June 5, 2025; accepted January 22, 2026)

Keywords: Young's modulus, and Poisson's ratio, solar tracking mechanism, SolidWorks CAD software, MSC.Marc finite element analysis software

In this study, we aimed to design and simulate a cost-effective and structurally simple dual-axis solar tracking mechanism. A crucial aspect of the research was to ensure the system's robustness against strong typhoons and earthquakes. The initial phase involved using SolidWorks Computer-Aided Design (CAD) software to perform operational interference checks. Each part was designed at a 1:1 scale, followed by 3D solid modeling and assembly simulations to verify the proper functioning of all components within the system. Static structural analysis was conducted using MSC.Marc finite element analysis software. The analysis mode was set to elastic-plastic, with selected materials being aluminum and steel, characterized by their density, Young's modulus, and Poisson's ratio. Boundary conditions fixed the displacement at the base plate and foundation bolt holes, while load conditions included wind pressure from a Category 17 typhoon and gravitational acceleration from a magnitude 5 earthquake. Upon the completion of the design, detailed manufacturing drawings were created using AutoCAD. These drawings included precise annotations of component dimensions and tolerances, ensuring accuracy during the fabrication process. This comprehensive approach ensures that the dual-axis solar tracking mechanism is both efficient and resilient under severe environmental conditions.

1. Introduction

A comprehensive solar tracking mechanism requires several essential components to maximize its efficiency. First, it needs a photovoltaic energy conversion and storage system, consisting of receivers, concentrators, and electromechanical equipment, to convert solar energy into electricity. Second, it should include a solar tracking structure that enables solar panels to follow the trajectory of the sun, ensuring optimal exposure to sunlight throughout the day. The

*Corresponding author: e-mail: jammy@nkust.edu.tw
*Corresponding author: e-mail: cfyang@nuk.edu.tw
https://doi.org/10.18494/SAM5785

ISSN 0914-4935
https://myukk.org/

relationship between a solar tracking mechanism and sensors is crucial, with sensors playing a pivotal role in such systems.[1–3] These sensors typically include solar irradiance meters, photovoltaic sensors, or other types of positional sensor, designed to precisely measure the sun's position and the intensity of sunlight. Specifically, sensors regularly scan the sky to determine the sun's position and trajectory. Based on the sensing theorem, the solar tracking mechanism should integrate sensor components to accurately track the sun's position. These sensors are crucial for continuously adjusting the orientation of the solar panels to maintain alignment with the sun's path across the sky. An advanced control system is necessary to manage the captured electrical energy effectively. It can accurately calculate how solar panels should adjust their orientation and tilt angles to maximize solar absorption. This control system ensures that the generated electricity is utilized efficiently, directing it to storage or immediate use based on real-time conditions and energy demands.

Such adjustments enable the solar system to dynamically adapt to changes in the sun's position, ensuring optimal performance in real time. In addition to tracking the sun's position, sensors can monitor other factors that affect the efficiency of solar energy systems, such as weather conditions and ambient light interference. This data helps optimize system operation, ensuring optimal energy collection efficiency under various conditions. Therefore, solar tracking mechanisms rely on advanced sensor technology. The sensors not only enable efficient solar energy harvesting but also enhance system reliability and automation capabilities. By integrating these components seamlessly, a solar tracking mechanism can significantly enhance the overall energy output and performance of solar installations, contributing to sustainable energy solutions.

From 1998 to 2000, Poulek and Libr addressed the problem of simplifying actuation and reducing system complexity by employing two small solar panels as tracking sensors in a single-axis solar tracking mechanism, using the generated electrical power to directly drive the tracking motion.[4,5] Clifford and Eastwood proposed a mechanical solution aimed at achieving passive tracking without electronic control, in which dual-layer aluminum–steel tubes filled with fluid were arranged on both sides of the pivot axis; the fluid's response to solar radiation induced rotational motion.[6] Abdallah and Nijmeh quantified the performance benefit of structural motion complexity, reporting that dual-axis tracking mechanisms can generate 41.34% more electricity than single-axis systems.[7,8] To improve control reliability and system integration, Al-Mohamad introduced a PLC-based control scheme that allowed photovoltaic modules to be configured in series or parallel while enabling automated solar tracking.[9] Mwithiga and Kigo focused on mechanical robustness and practical application, developing a solar tracking mechanism for a manual dryer using low-carbon steel absorber plates and polyvinyl chloride transparent covers, significantly reducing drying time from 5–7 days to 2 days.[10]

Aiuchi *et al.* investigated tracking accuracy under mechanical constraints, employing photovoltaic sensors in an equatorial-mount tracker and achieving an angular error within 0.02 radians, although performance degradation was observed under cloudy conditions.[11] Bakos examined mechanical transmission design, utilizing sprockets in a dual-axis tracking system to enhance structural reliability.[12] Barsoum explored power transmission efficiency, adopting belt-driven mechanisms and demonstrating that single-axis and dual-axis systems can improve

energy output by approximately 20% and more than 40%, respectively, compared with fixed installations.[13] Ray *et al.* addressed actuation coordination and control precision by using a microcontroller-driven dual-axis tracking system with multiple sensors and DC motors, achieving a 37% efficiency improvement while noting the trade-off between increased mechanical complexity and long-term energy gains.[14]

Upon determining research objectives, we proceeded to plan the design of a solar tracking mechanism. Initially, relevant literature on solar tracking mechanisms was gathered to serve as a reference for establishing the design criteria and goals of the intended solar tracking mechanism. With the functional design objectives defined, conceptual design followed to assess the feasibility of the proposed ideas. Subsequently, detailed design was undertaken to consider practical aspects such as manufacturing methods and component fabrication conditions. Each component was then modeled in 3D using SolidWorks software at a 1:1 scale. The verification of interference-free operation and the ability to rotate as required were ensured. Finally, the design underwent validation using the finite element analysis software MSC.Marc to confirm whether the mechanism's strength met expectations. This comprehensive approach ensured that the designed solar tracking mechanism not only met its intended goals but also adhered to structural integrity requirements.

2. Simulation Process and Parameters Used

In this study, we aimed to design a single-seat solar tracking mechanism capable of generating 1 kW of power. In this context, the term single-seat refers to a single mounting unit (or support pedestal) that integrates the mechanical structure, drive system, and control components to support and actuate a group of solar panels as a single tracking module. This configuration contrasts with multiseat or distributed systems, where each panel or panel pair is mounted and driven independently. The selected photovoltaic panels each have a maximum power output of 250 W; therefore, the proposed mechanism is designed to accommodate four panels, resulting in a total structural load of approximately 80 kg. Commercial solar photovoltaic systems are generally classified, according to their mechanical degrees of freedom, into fixed, single-axis, and dual-axis tracking systems. In this study, we focus on the design and simulation of a dual-axis solar tracking mechanism, which enables independent rotation in both the elevation and azimuth directions to maximize solar energy capture. With respect to solar position determination, several commonly used approaches are available. These approaches are based on different theoretical frameworks rather than individual formulas. Specifically, they include celestial coordinate-based methods (e.g., ecliptic, equatorial, and horizontal coordinate systems) and time-based analytical formulations that are used to compute solar zenith, elevation, and azimuth angles. In this work, instead of deriving tracking angles from analytical formulas, solar time and position data published by the Taiwan Central Weather Bureau are directly adopted as reference inputs, ensuring accurate and reliable tracking coordinates throughout the day. Common approaches to obtain the sun's position include celestial coordinate-based methods (e.g., ecliptic, equatorial, and horizontal coordinate systems) and time-based analytical formulations that compute solar elevation and azimuth angles. In this study, solar time/position

data published by the Taiwan Central Weather Bureau are directly adopted as reference inputs to provide reliable tracking coordinates. There are several calculation formulas for tracking the sun's angle, as follows: (1) celestial coordinate systems, including ecliptic, equatorial, and horizontal coordinate systems, and (2) sun position calculation, involving the calculation of solar time and its relationship to the equator to determine solar zenith angle, elevation angle, and azimuth angle.

In this study, we adopted the method of tracking the sun based on elevation and azimuth angles, directly referencing solar time data published by the Taiwan Central Weather Bureau for precise tracking coordinates. This approach ensured that the system accurately aligns with the sun's path, optimizing energy collection efficiency throughout the day. Owing to space constraints, the mechanism was designed beneath the solar panels, utilizing a circular support structure and track for azimuthal rotation, and the schematic is shown in Fig. 1(a). The elevation axis was positioned below the solar panels, imposing angular limitations on the tracking mechanism during rotation. The radial spatial constraint around the elevation rotation mechanism necessitated splitting the support structure into upper and lower segments. To achieve the required elevation tracking angles, the upper segment of the support structure employed two square pipes connected to the solar panel truss framework. The lower segment enhanced the structural strength of the rotating support with four circular pipes. The control system components were housed within the support structure, and a rotating disc integrated within the rotating support mechanism drove the elevation rotation mechanism. This configuration optimized both spatial utilization and structural integrity while ensuring precise solar tracking capabilities to maximize energy generation efficiency.

Figure 1(b) shows the complete assembly diagram. The detailed design begins with processing sequence and methods. The solar panel was positioned directly above the mechanism. To minimize the additional motor load during elevation angle rotation, low-density aluminum was chosen over steel for its lighter weight. Aluminum square tubes were initially considered but lacked the strength to withstand wind pressures equivalent to a Category 17 typhoon, hence

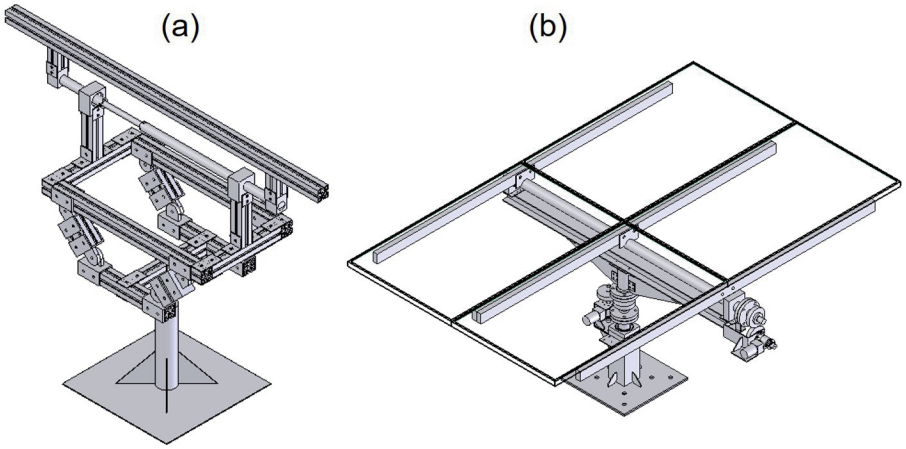

Fig. 1. (a) Solar tracking mechanism and (b) detailed assembly.

aluminum extrusions were chosen. For the elevation angle support structure, it consisted of an elevation rotation axis and an elevation main beam. The elevation main beam bore the load of all components above it and was made from steel owing to strength requirements.

Figures 2(a) and 2(b) show the enlarged views of the elevation rotation and azimuth rotation mechanisms, respectively. According to the assembly configuration, the mechanisms are decomposed into individual components and labeled with distinct part numbers. Part A represents the structural frame used to secure the solar panel. Part B denotes the elevation rotation shaft, Part C is the passive gear shaft, Part D corresponds to the main beam of the elevation structure, and Part E is the mounting bracket for the elevation motor. Parts F, G, and H constitute the rotation shafts of the azimuth mechanism, whereas Parts I and J serve as the corresponding shaft support bases. Part K represents the motor mounting base of the azimuth rotation mechanism.

MSC.Marc is an advanced nonlinear finite element analysis software used in this study as the analytical tool. In this study, we focus on static structural analysis under normal operating conditions. Although the environmental temperature of the mechanism may vary from 20 to 40 °C, the materials used in the structure exhibit low coefficients of thermal expansion, and the resulting thermal deformation within this temperature range remains well within the allowable mechanical tolerances of the mechanism. Consequently, the induced thermal expansion does not lead to notable changes in load distribution, stress level, and operational functionality. Therefore, the effects of temperature variation on material properties and structural behavior were considered negligible for the purposes of this study and were not explicitly included in the simulation. Material properties were defined only at room temperature, including Young's modulus, Poisson's ratio, and density, as listed in Table 1. As shown in Fig. 1(b), the four fitting materials of the above mechanism were made of aluminum alloy 6061, whereas the rest [Fig. 1(a)] were made of steel A36.

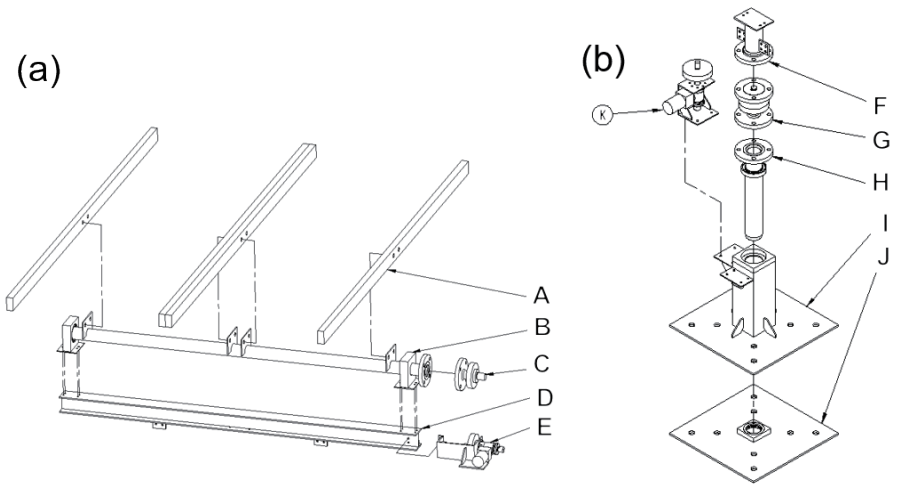

Fig. 2. Enlarged views of (a) elevation rotation and (b) azimuth rotation mechanisms.

Table 1
Coefficients of the materials used.

Material	A36 steel	6061 aluminum
Young's modulus (GPa)	190	70
Poisson's ratio	0.30	0.33
Density (kg/m^3)	7850	2710

3. Simulation Results and Discussion

The preliminary mesh partitioning was performed using the Workbench meshing module, with divisions based on specific regions: one section for the connection between the H-beam and the left and right bearing seats, and another for the middle part connected to the supporting structure. The number of elements was uniform across these three sections, with specified element edge lengths of 4.5, 4.0, 3.5, 3.0, 2.7, 2.5, 2.3, and 2.0 mm. The remaining areas were generated outwardly at a growth rate of 1.2. The resulting mesh counts sequentially were 525592, 568379, 646529, 769366, 867563, 998695, 1157574, and 1472585. Subsequently, the Workbench mesh files were imported into MSC.Marc for detailed processing. This meticulous meshing approach ensures that the structural model captured the intricacies of stress and displacement patterns accurately, providing insights into how the design responds to operational conditions. The various mesh densities in different regions allow for a comprehensive evaluation of structural behavior under mechanical loading and environmental stresses. Such detailed analysis is crucial for optimizing the design's performance and ensuring its resilience under expected operational scenarios. In this study, we employed tetrahedral four-node low-order elements for convergence analysis, with analysis points positioned on the H-beam. The corresponding node locations are depicted in Fig. 3, focusing on a point on the cross-sectional area of the H-beam to observe convergence behavior.

The mesh diagram is depicted in Fig. 4, which illustrates the finite-element mesh layout used in the analysis. As shown in the figure, the mesh is locally refined in critical regions, particularly around the connections between the H-beam and the supporting structures, where higher stress gradients are expected. Toward the outer regions, the mesh density is gradually reduced to improve computational efficiency while maintaining numerical accuracy. Figure 5 shows the mesh convergence curve, demonstrating that the mesh begins to converge as the number of elements approaches 769366, and achieves convergence within 1% by 867563 elements. This convergence behavior indicates that the selected mesh density is appropriate for capturing the structural response with sufficient accuracy. Therefore, a mesh configuration consisting of 998695 elements and 211865 nodes was selected to accurately model the structural components. The denser mesh near critical connections ensures that stress concentrations and displacement gradients are adequately resolved, contributing to reliable predictions of structural performance under operational conditions. Such detailed meshing and convergence analysis are essential in ensuring the robustness and reliability of structural simulations, providing valuable insights for optimizing design parameters and enhancing overall structural integrity. Thus, the choice of the number of elements and the incremental growth rate were crucial in achieving a balance between computational efficiency and accuracy. By analyzing the mesh counts and their corresponding

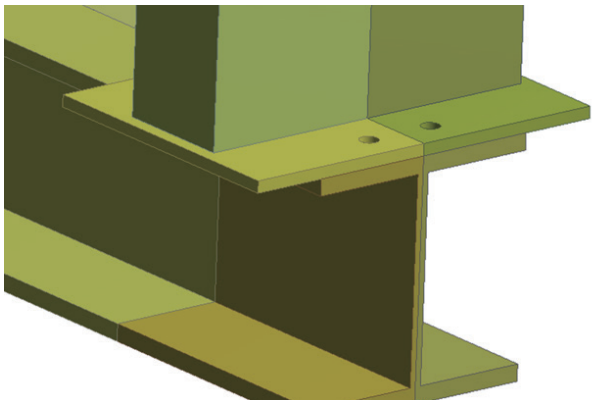

Fig. 3. (Color online) Locations for corresponding nodes.

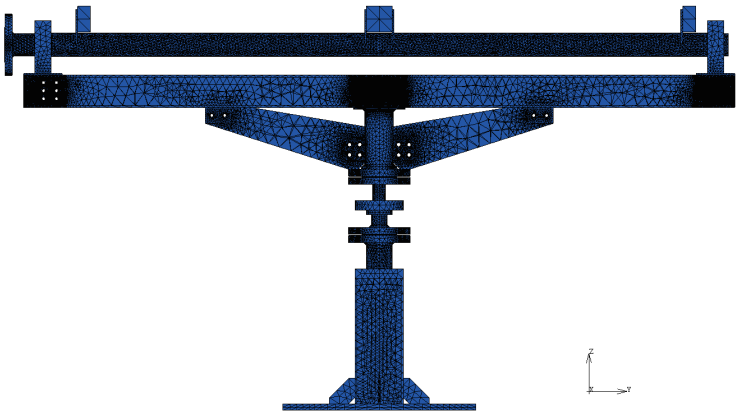

Fig. 4. (Color online) Mesh diagram.

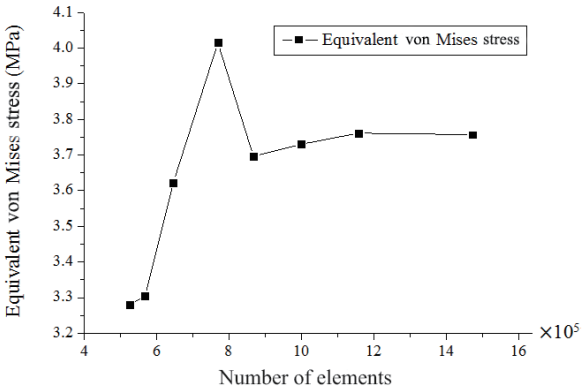

Fig. 5. Variation for mesh convergence.

stress results, it is evident that a mesh configuration with approximately 867563 elements is sufficient to ensure accurate simulation outcomes without unnecessarily increasing the computational load.

Figure 6 depicts the stress field distribution in this study's structural analysis. The color gradient ranges from blue indicating minimal stress to purple, orange, and yellow indicating increasing stress levels. The overall structure shows a predominantly blue stress distribution, indicating lower stress levels across most areas. Areas of stress concentration are observed near holes and at welded joints, typical stress concentration points in structural components. Specifically, owing to the structural design where the H-beam lacks direct support from the floor on its left and right sides and relies solely on rotational mechanisms at the center, stress concentrations are evident at the bearing seats located at both ends of the beam. Understanding these stress concentrations is crucial for optimizing the structural design to ensure uniform stress distribution and minimize potential failure points. By identifying and mitigating stress concentrations, engineers can enhance the structure's durability and performance under operational conditions, ensuring that it meets safety and reliability standards. This comprehensive stress analysis provides valuable insights into the structural behavior, guiding improvements for enhanced structural integrity and operational efficiency.

In this study, the structural stress distribution analysis reveals a gradient from blue indicating minimal stress to purple, orange, and yellow indicating increasing stress levels. Notably, the absence of yellow regions in the overall stress map prompts a closer examination of localized stress concentrations. Figure 7 illustrates that the highest stress occurs at the furthest hole from the rotational center of the mechanism, situated on the motor mount. Although the holes on the motor mount are farther from the center compared with those on the H-beam, the maximum stress point is observed on the H-beam. This is because the H-beam bears the entirety of the loads imposed by the mechanism above it. The maximum stress recorded on the H-beam is 27 MPa, which is below the yield strength of the material (245 MPa). This finding indicates that the structural design is robust enough to withstand severe environmental conditions. Specifically, the structure's strength is deemed adequate to endure a Category 17 typhoon and a magnitude 5

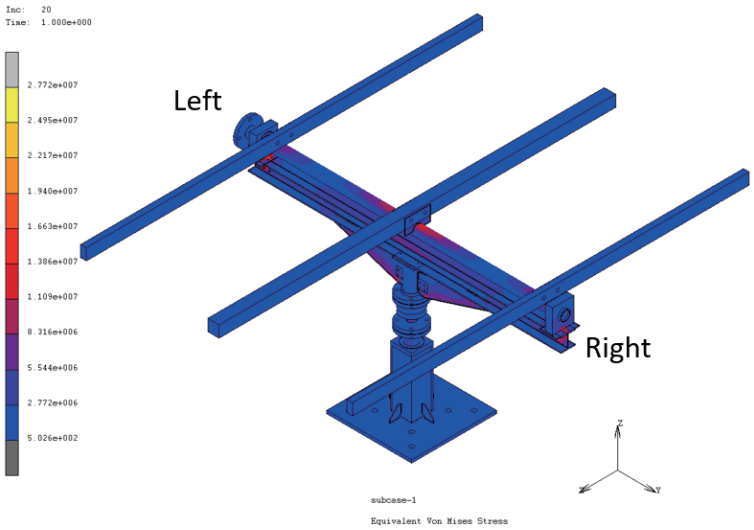

Fig. 6. (Color online) Overall structural diagram for stress field distribution.

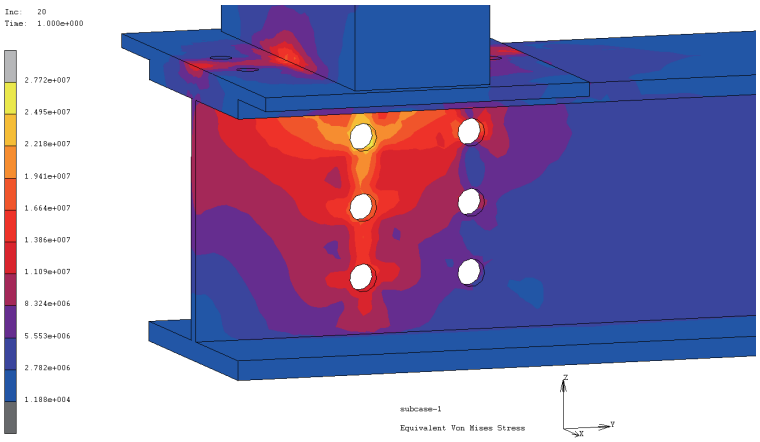

Fig. 7. (Color online) Local magnification diagram for stress distribution.

earthquake, affirming its reliability under extreme operational scenarios. This analysis underscores the importance of detailed stress evaluation in optimizing structural design for safety and performance requirements. The convergence analysis underscores the importance of selecting an optimal mesh size to avoid excessive computational time and resources while maintaining the precision of the results. The maximum stress of 27 MPa, being significantly lower than the material's yield strength, confirms that the H-beam design is structurally sound under the given loading conditions.

Figure 8 illustrates the displacement field distribution of the structure in this study, providing a visual representation of how the mechanism deforms under load. The color gradient from blue to yellow indicates various levels of displacement, with blue representing minimal displacement and yellow indicating maximum displacement. The primary area of deformation was observed on the extrusion, particularly at the end of the central extrusion where the maximum displacement reached 1.9 mm. This suggests that the structural response is concentrated and localized, which is crucial for understanding the mechanical behavior and potential stress points of the mechanism. This displacement pattern is significant as it informs engineers and researchers about where the structure is most susceptible to deformation and potential failure under operational conditions. By pinpointing areas of high displacement, designers can optimize the structure's geometry, material choices, or operational parameters to enhance its performance and reliability. Moreover, the color-coded visualization in Fig. 7 allows for a clear interpretation of how deformation propagates throughout the structure.

The different colors shown in Fig. 8 indicate various levels of displacement, providing further insights into the mechanical response and strain distribution across different parts of the designed system. Figure 8 not only showcases the deformation pattern of the structure but also serves as a valuable tool for discussing and analyzing the mechanical behavior and performance optimization of the mechanism under study. To verify the practical applicability of the proposed single-seat dual-axis solar tracking system, the design has been physically fabricated and implemented in prior work.[15] Through multiple iterations of prototype development, continuous refinement via 3D modeling, and repeated design evaluations, the final structure of the dual-axis

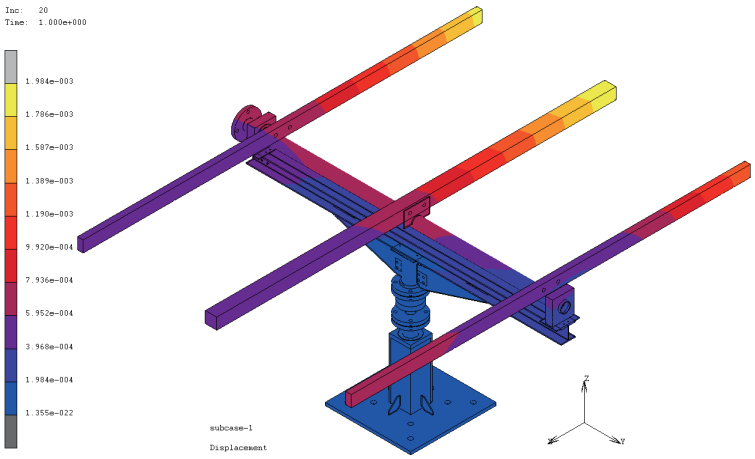

Fig. 8. (Color online) Overall structural diagram for displacement field distribution.

tracking mechanism was successfully completed and validated. A key design consideration was compatibility with commercially available standard components, which significantly reduced the need for custom-fabricated parts and enabled effective cost control. Moreover, the entire structure was designed to be modular and can be disassembled, facilitating transportation and on-site installation. The assembly process was straightforward and could be completed by a small number of workers, demonstrating that the proposed mechanism is not merely theoretical but is suitable for real-world deployment.

4. Conclusions

In this study, the number of elements was uniformly defined using element edge lengths of 4.5, 4.0, 3.5, 3.0, 2.7, 2.5, 2.3, and 2.0 mm. The remaining areas were generated outwardly at a growth rate of 1.2. The resulting mesh counts sequentially were 525592, 568379, 646529, 769366, 867563; 998695, 1157574, and 1472585. A mesh configuration consisting of 998695 elements and 211865 nodes was selected to accurately model the structural components. The mesh began to converge as the number of elements approached 769366 and achieved convergence within 1% by 867563 elements. This convergence indicates that further refinement beyond this point yielded diminishing returns in terms of accuracy. The simulation results demonstrated that the maximum stress recorded on the H-beam was 27 MPa, which is well below the yield strength of the material, specified as 245 MPa.

Acknowledgments

This research was supported by projects under Nos. NSTC 113-2622-E-390-001 and NSTC 113-2221-E-390-011.

References

1 C. Jamroen, C. Fongkerd, W. Krongpha, P. Komkum, A. Pirayawaraporn, and N. Chindakham: Appl. Energy **299** (2021) 117295.
2 U. Mamodiya and N. Tiwari: Comput. Electr. Eng. **111** (2023) 108920.
3 A. Jose, R. M. Varghese, R. Mathew, and P. V. Sujit: Int. Conf. Communication, Embedded-VLSI Systems for Electric Vehicle (ICCEVE 2023) (Hybrid Conference, Kottayam, India) (2023) pp. 90–92.
4 V. Poulek and M. Libr: Sol. Energy Mater Sol. Cells **l51** (1998) 113.
5 V. Poulek and M. Libr: Sol. Energy Mater Sol. Cells **l60** (2000) 99.
6 M. J. Clifford and D. Eastwood: Sol. Energy **77** (2004) 269.
7 S. Abdallah: Energy Convers. Manag. **45** (2004) 1671.
8 S. Abdallah and S. Nijmeh: Energy Convers. Manag. **45** (2004) 1931.
9 A. Al-Mohamad: Appl. Energy **79** (2004) 345.
10 G. Mwithiga and S. N. Kigo: J. Food Eng. **74** (2006) 247
11 K. Aiuchi, K. Yoshida, M. Onozaki, Y. Katayama, M. Nakamura, and K. Nakamura: Sol. Energy **80** (2006) 1089.
12 G. C. Bakos: Renew. Energ. **31** (2006) 2411.
13 N. Barsoum: Third UKSim European Symposium on Computer Modeling and Simulation (Athens, Greece) (25–27 Nov, 2009) pp.23–30.
14 S. K. Ray, M. A. Bashar, M. Ahmad, and F. B. Sayed: Global J. Resear. Eng. **12** (2012) 29.
15 H. S. Chen, X. Q. Lin, C. M. Hsu, and C. F. Yang: Sens. Mater. **37** (2025) 2421.